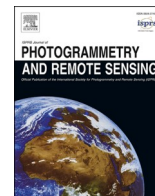


Contents lists available at [ScienceDirect](https://www.sciencedirect.com)

ISPRS Journal of Photogrammetry and Remote Sensing

journal homepage: www.elsevier.com/locate/isprsjprs

Statistical estimation of next-day nighttime surface urban heat islands

Jiameng Lai^a, Wenfeng Zhan^{a,b,*}, Jinling Quan^c, Benjamin Bechtel^d, Kaicun Wang^e, Ji Zhou^f, Fan Huang^a, Tirthankar Chakraborty^g, Zihan Liu^a, Xuhui Lee^g^a Jiangsu Provincial Key Laboratory of Geographic Information Science and Technology, International Institute for Earth System Science, Nanjing University, Nanjing, Jiangsu 210046, China^b Jiangsu Center for Collaborative Innovation in Geographical Information Resource Development and Application, Nanjing 210023, China^c State Key Laboratory of Resources and Environmental Information System, Institute of Geographic Sciences and Natural Resources Research, Chinese Academy of Sciences, Beijing 100101, China^d Department of Geography, Ruhr-University Bochum, 44801 Bochum, Germany^e State Key Laboratory of Earth Surface Processes and Resource Ecology, College of Global Change and Earth System Science, Beijing Normal University, Beijing 100875, China^f School of Resources and Environment, University of Electronic Science and Technology of China, Chengdu 611731, China^g School of Forestry and Environmental Studies, Yale University, New Haven, CT 06511, USA

ARTICLE INFO

Keywords:

Surface urban heat island
Thermal remote sensing
Land surface temperature
MODIS
Support vector regression

ABSTRACT

Estimating future temporal patterns of Surface Urban Heat Islands (SUHIs) on multiple time scales is an ongoing research endeavor. Among these time scales, estimation of next-day SUHIs is of special significance to urban residents, yet we currently lack a simple but efficient approach for making such estimations. In the present study, we propose a statistical strategy for estimating next-day nighttime SUHIs, based on incorporating various SUHI controls into a support vector machine regression (SVR) model. The majority of both the surface controls (including factors related to land cover and solar radiation) and meteorological controls (including temperature fluctuations, relative humidity, accumulated precipitation, wind speed, aerosol optical depth, and soil moisture) that have previously been found to account for daily SUHI variations were used as estimators, and we provide estimations for both the overall SUHI intensity (SUHII) and pixel-by-pixel Gaussian-based LSTs over 59 Chinese megacities. For the overall SUHII, the mean absolute error (MAE) is 0.67 K on average, and the mean absolute percentage error (MAPE) is no more than 25% for more than 90% of the cities. For the pixel-by-pixel LSTs, the associated MAE is less than 2.0 K in most scenarios. In addition, the contribution from each selected estimator to SUHII estimation is assessed comprehensively. Among all the estimators, the contribution from relative humidity is the greatest, followed by rural surface temperature and surface air temperature. Moreover, for nearly 78% of the cities, the estimators related to day-to-day SUHI variations make a larger contribution than those related to intra-annual SUHI variations. We conclude that our simple yet effective statistical approach for estimating next-day SUHIs can potentially help urban residents to better adapt to urban heat stress.

1. Introduction

The Urban Heat Island (UHI), the phenomenon of elevated urban temperatures referenced to rural temperatures, is a widespread outcome of urbanization (Oke, 1982; Oke et al., 2017). Increasing attention has been paid to the UHI in the past few decades (Chakraborty et al., 2020; Chakraborty and Lee, 2019; Clinton and Gong, 2013; Hu and Brunsell, 2015; Maimaitiyiming et al., 2014; Nichol et al., 2009; Nichol and To, 2012; Pichierri et al., 2012; Stewart and Oke, 2012; Wang et al., 2017),

mostly because of its direct impacts on human thermal comfort and the urban environment (Gong et al., 2012; Grimm et al., 2008; Knapp et al., 2010).

Studies of UHIs can generally be classified into two categories: UHIs within the canopy layer (canopy layer UHI, CUHI) and those within the surface layer (surface UHI, SUHI). CUHI studies have greatly benefited from the rapid development of climate modelling, as well as high-frequency sampling of the surface air temperature (SAT) (Lee et al., 2016; Oke, 1981; Oke et al., 2017; Runnalls and Oke, 2000; Steeneveld

* Corresponding author at: Nanjing University at Xianlin Campus, No. 163, Xianlin Avenue, Qixia District, Nanjing, Jiangsu Province 210023, China.

E-mail addresses: zhanwenfeng@nju.edu.cn (W. Zhan), quanjl@reis.ac.cn (J. Quan), benjamin.bechteler@rub.de (B. Bechtel), kcwang@bnu.edu.cn (K. Wang), jzhou233@uestc.edu.cn (J. Zhou), tc.chakraborty@yale.edu (T. Chakraborty), xuhui.lee@yale.edu (X. Lee).<https://doi.org/10.1016/j.isprsjprs.2021.04.009>

Received 2 December 2020; Received in revised form 11 April 2021; Accepted 13 April 2021

0924-2716/© 2021 International Society for Photogrammetry and Remote Sensing, Inc. (ISPRS). Published by Elsevier B.V. All rights reserved.

et al., 2011). The SUHI, by comparison, cannot be well represented by climate modelling or point-based measurements, due to its greater spatiotemporal variability. As a result, studies focusing on the SUHI were largely unavailable until the advent of periodically and spatially continuous satellite-based land surface temperature (LST) observations (Chakraborty and Lee, 2019; Feng and Myint, 2016; Fu and Weng, 2018; Huang and Wang, 2019; Imhoff et al., 2010; Keramitsoglou et al., 2011; Meng et al., 2018; Nichol, 2009; Schwarz et al., 2011; Shen et al., 2016; Voogt and Oke, 2003; Weng, 2009; Weng and Fu, 2014; Yang et al., 2015; Yang et al., 2017).

Recently, there have been an increasing number of studies focusing on the modelling of SUHIs (Zhou et al., 2019). An indispensable step towards SUHI modelling is the identification of the factors that contribute to their variations. Previous studies have clarified that the SUHI temporal variations can be separated into several components at different time scales (Fu and Weng, 2016; Quan et al., 2016), and diverse factors have been suggested as controls for these SUHIs on different scales. On the *long-term* scale (i.e., the inter-annual scale), factors related to the intensity of urban development, land cover changes, and climatic conditions, are the most important (Chen et al., 2006; Lin et al., 2018; Shen et al., 2016; Silva et al., 2018; Ward et al., 2016; Yao et al., 2017; Zhao et al., 2014). On the *mid-term* scale (i.e., the intra-annual scale), SUHI variations are dominated by land cover status, urban structures, anthropogenic heat release, and climatic conditions (Cao et al., 2016; Du et al., 2016; Imhoff et al., 2010; Lazzarini et al., 2013; Liao et al., 2017; Qiao et al., 2013; Zhao et al., 2014). On the *short-term* scale (i.e., the daily scale), weather conditions exert the greatest impact (Lai et al., 2021; Quan, 2014; Shaposhnikova, 2018; Zhou et al., 2011). On an even shorter scale (i.e., the diurnal scale), vegetation status, urban forms, and weather conditions, all make considerable contributions to SUHI variations (Lai et al., 2018). A combination of these different categories of factors can substantially advance the modelling of the SUHI temporal patterns over past periods (Li et al., 2019; Schwarz and Manceur, 2015; Wang et al., 2015; Ward et al., 2016; Weng et al., 2004; Xu et al., 2018; Zhou et al., 2011; Zhou et al., 2013; W. Zhou et al., 2014; Zhou et al., 2017). By contrast, estimating the future SUHI is relatively difficult, mainly because most of the future status of these SUHI-related factors are more difficult to estimate and therefore are unable to serve as estimators (Mushore et al., 2017).

Nevertheless, by integrating models that can estimate future land cover changes, several studies have estimated the future SUHI for several case cities: e.g., in Dhaka through the year of 2019 and 2029 (Ahmed et al., 2013), in Hanoi through the year 2023 (Tran et al., 2017), in Harare through 2025, 2035, and 2045 (Mushore et al., 2017), and in Babol through 2045 (Firozjaei et al., 2018). Notably, land cover changes are significant only on the annual/seasonal scale, and therefore the future SUHIs estimated by this strategy are restricted to *long-term/mid-term* scales. A more effective adaptation to urban extra stress requires the estimation of SUHIs in the very near future and with a larger temporal variability: e.g., the daily SUHI on a *short-term* scale. However, the estimation of *short-term* SUHIs (e.g., next-day SUHI estimation) remains challenging, largely because of the high spatiotemporal heterogeneity of LSTs, together with insufficient understanding of the factors controlling *short-term* SUHIs.

SUHI variations (especially for nighttime) on the *short-term* scale have in some cities been shown to be predominantly influenced by changes in weather conditions (Feng et al., 2019; Quan, 2014; Shaposhnikova, 2018; Zhou et al., 2011). More recently, on a continental scale, Lai et al. (2021) decomposed the *short-term* variations of nighttime SUHIs into two components - *mid-term* and day-to-day SUHIs - and in addition a comprehensive investigation of the factors controlling both components was conducted. The results revealed that for the *mid-term* component of nighttime SUHIs, factors related to land cover and solar radiation contribute the most; whereas for the day-to-day SUHIs, dominant controls from weather conditions, including relative humidity, accumulated precipitation, temperature fluctuations, wind speed,

soil moisture and aerosol optical depth (AOD), were demonstrated (Lai et al., 2021).

These previous studies have together improved our understanding of the mechanisms of nighttime SUHI variations on the *short-term* time-scale. More importantly, due to the advancement of weather forecasting techniques, the next-day values of some key meteorological variables that contribute to *short-term* nighttime SUHIs (e.g., relative humidity, precipitation, wind speed and surface air temperature (Quan, 2014; Zhou et al., 2011)) can be predicted with high accuracy (Bauer et al., 2015). This significantly raises the prospect of incorporating these variables as estimators and lays the foundations for estimation of next-day nighttime SUHIs.

The present study proposes a statistically robust strategy which addresses the difficulty of estimating next-day nighttime SUHIs. Various factors that were reported closely related to the daily SUHI variations were used as estimators. They include the factors related to land cover, solar radiation, temperature, relative humidity, accumulated precipitation, wind speed, aerosol optical depth, and soil moisture (Feng et al., 2019; Lai et al., 2021; Quan, 2014; Shaposhnikova, 2018; Zhou et al., 2011). By incorporating these estimators into a support vector machine regression (SVR) model, the estimation accuracy was examined and the contribution from each estimator was further evaluated. We demonstrate that our simple statistical approach is easily implemented and applicable to other cities, and therefore it can help bridge the knowledge gap in next-day SUHI estimation.

2. Study area

Mainland China was selected as the study area due to the reported widespread occurrence of the SUHI phenomenon (D. Zhou et al., 2014). A total of 59 cities were chosen (Fig. 1), based on a series of criteria including urban area (>100 km²), the availability of weather station data (at least one weather station must exist within the administrative boundary), and sufficient numbers of valid daily nighttime SUHI observations (we adapted the criterion that there must be at least 50 valid observations for each city for an entire year). The cities are distributed within six different climatic zones (Zheng et al., 2010). For a further demonstration of the estimated pixel-by-pixel LST results (see Section 3.2 for more details), we selected six megacities located in the six climatic zones. These six megacities are: Harbin (HRB), Xi'an (XA), Lhasa (LS), Nanjing (NJ), Kunming (KM), and Nanning (NN) (Fig. 1). The delineation of urban and rural areas for each city was according to the MODIS land cover product (see Section 3.1.1). The classified 'urban and built-up' pixels were aggregated as urban areas, and the aggregation distance was set as 2 km (D. Zhou et al., 2014), then the rural areas were defined as the 15-km buffer zone of the urban areas (Bechtel, 2015).

3. Data and methodology

3.1. Data

3.1.1. MODIS data

The LST, land cover type, normalized difference in vegetation index (NDVI), aerosol optical depth (AOD), and albedo products from MODIS for 2012 were employed in this study (see Table 1). The LST data were obtained from the MOD11A1 (from Terra satellite) and MYD11A1 (from Aqua satellite) products (with a spatial resolution of 1 km). The MODIS LST data were ensured to have a good degree of accuracy using the generalized split-window algorithm (Wan, 2008). We only used the nighttime data, considering the lower uncertainty induced by surface thermal anisotropy at night, and the demonstrated significant meteorological controls on nighttime SUHIs. The LST images from the Terra and Aqua satellites were aggregated each day to minimize the impacts from data gaps. For the aggregated images, those with more than 50% cloudy urban/rural pixels were excluded from further analysis (Huang et al., 2019). Yearly land cover type data were derived from the

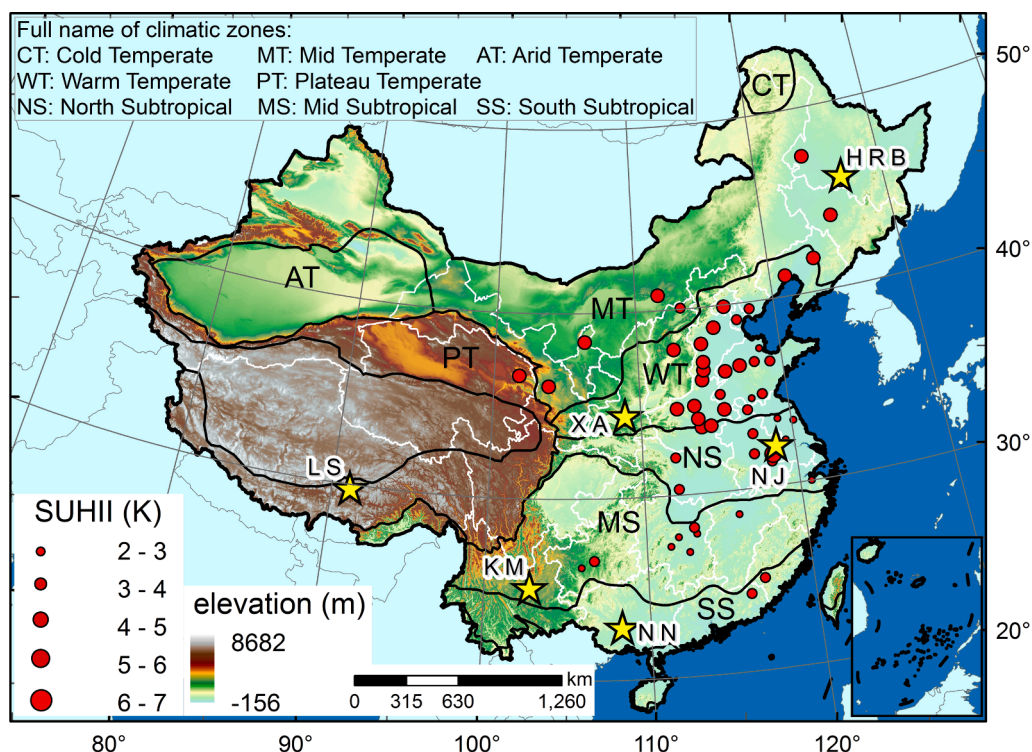


Fig. 1. Distribution of cities within the study area. The red dots represent the locations of the 59 megacities, with dot size denoting their annual mean nighttime SUHII intensity (SUHII) in 2012. HRB (Harbin), XA (Xi'an), LS (Lhasa), NJ (Nanjing), KM (Kunming), and NN (Nanning) are the six representative cities used for further demonstration of pixel-by-pixel estimations. (For interpretation of the references to color in this figure legend, the reader is referred to the web version of this article.)

Table 1
Information on the satellite and *in-situ* data used in this study.

Data type	Data source	Spatial resolution	Temporal resolution
LST	MOD/ MYD11A1	1 km	daily
land cover	MCD12Q1	500 m	yearly
NDVI	MOD/ MYD13A3	1 km	monthly
AOD	MOD/ MYD04_3K	3 km	daily
albedo	MCD43C3	0.05 degree	16-day
SAT	<i>in-situ</i>	point-based	daily
relative humidity	<i>in-situ</i> observation	point-based	daily
wind speed	<i>in-situ</i> observation	point-based	daily
accumulated precipitation	<i>in-situ</i> observation	point-based	daily

MCD12Q1 product (with a resolution of 500 m), and a total of 17 land cover types were identified under the International Geosphere-Biosphere Program (IGBP) classification scheme. The spatial resolution of land cover type was resampled to 1 km to match the LST product, using the nearest neighbor strategy (Clinton and Gong, 2013). The NDVI data were derived from the MOD13A3 (from Terra satellite) and MYD13A3 (from Aqua satellite) products (with a resolution of 1 km). The AOD data were retrieved at 660 nm, obtained from the MOD04_3K (from Terra satellite) and MYD04_3K (from Aqua satellite) products (with a resolution of 3 km). For the NDVI and AOD data, the images from the Terra and Aqua satellites were also aggregated each day. The albedo data were the black sky albedo (BSA) in the shortwave band (0.3–5.0 μm) extracted from the 16-day MCD43C3 product (with a resolution of 0.05°).

3.1.2. In-situ data

In-situ measurements used include daily mean surface air temperature (SAT), relative humidity, wind speed, and accumulated precipitation (Table 1), obtained from 449 weather stations in the selected cities. Note that the daily accumulated precipitation corresponds to the total amount of precipitation during an entire diurnal cycle from 20:00 to 20:00 (local time) of the next day. All of the meteorological data were derived from the China Meteorological Administration (CMA, <http://www.cma.gov.cn>); all of them have undergone a series of quality controls, including assessment of climatic range, internal and spatio-temporal consistency, and man-machine interaction (Ren et al., 2015).

3.2. Methodology

The first step in achieving a statistical estimation of next-day nighttime SUHIs is to quantify appropriately the SUHIs. Both the overall SUHI intensity (i.e., the SUHII) as well as its spatial patterns (i.e., the pixel-by-pixel LSTs) were quantified for estimation (see Section 3.2.1). We then selected various factors that contribute to the nighttime SUHI variations on the *short-term* time scale (daily scale), as already identified partly by previous studies (Lai et al., 2021; Quan, 2014; Zhou et al., 2011), as estimators for the next-day SUHIs (see Section 3.2.2). All of the estimators were then incorporated into an SVR model to estimate the next-day SUHIs for each single city (see Section 3.2.3). Finally, the contributions from these input estimators were quantified to obtain a better understanding of their performance in estimation (see Section 3.2.4).

3.2.1. SUHI quantification by the Gaussian model

We used the frequently used Gaussian model proposed by Streutker (2002) to facilitate characterization of the SUHIs, given (1) its recognized efficiency and stability for simulating both the intensity and overall feature of the nighttime SUHIs (Anniballe and Bonafoni, 2015; Quan et al., 2014; Tran et al., 2006; Zhou et al., 2011), and (2) its

relatively low susceptibility to data gaps induced by clouds.

The SUHI characterization with the Gaussian model complied with the following three steps: First, the rural LSTs were fitted into a planar surface using Eq. (1). Then the SUHI signature was extracted as the difference between the urban and the fitted rural LSTs, according to Eq. (2). Finally, the SUHI signature extracted by Eq. (2) was fitted to a Gaussian surface, using Eq. (3).

$$T_r(x, y) = T_0 + a_1x + a_2y \quad (1)$$

where $T_r(x, y)$ denotes the LST for a rural pixel at the location (x, y) ; T_0 is the rural mean surface temperature; and a_1 and a_2 are two coefficients.

$$\Delta T(x, y) = T_u(x, y) - T_r(x, y) \quad (2)$$

where $\Delta T(x, y)$ denotes the SUHI signature for the urban pixel at the location (x, y) ; $T_u(x, y)$ is the LST for this urban pixel; and $T_r(x, y)$ denotes the fitted rural LST for this pixel, which is derived from Eq. (1).

$$\begin{cases} \Delta T = a_0 \cdot \exp\left(-\frac{1}{2}U\right) \\ U = \{a_x^{-1} \cdot [(x - x_0)\cos\phi + (y - y_0)\sin\phi]\}^2 + \{a_y^{-1} \cdot [(y - y_0)\cos\phi - (x - x_0)\sin\phi]\}^2 \end{cases} \quad (3)$$

where a_0 is the maximum SUHI intensity (SUHII); a_x and a_y represent the half long and short axes of the Gaussian-simulated SUHI ellipse; (x_0, y_0) denotes the location of the SUHI centroid; and ϕ represents the orientation of the Gaussian-simulated SUHI ellipse.

To reduce the possible uncertainties induced by the Gaussian modelling, we evaluated the modelling performance using the correlation coefficient (r) and root-mean-square error ($RMSE$) between the Gaussian-simulated and the original LSTs. All the results with the $r < 0.7$ or $RMSE > 1.0$ K were recognized as inaccurately modelled (Lai et al., 2021) and were therefore excluded from further analysis. For the remaining valid results, the SUHII (I) and the pixel-by-pixel Gaussian-based LSTs (T_G) were then obtained with the following equation:

$$\begin{cases} I = a_0 \\ T_G(x, y) = \Delta T(x, y) + T_r(x, y) \end{cases} \quad (4)$$

where I is the SUHII; a_0 is the parameter derived from Eq. (3); $T_G(x, y)$ is the Gaussian-based LST for a certain pixel located at coordinate (x, y) ; $\Delta T(x, y)$ is the Gaussian-fitted SUHI feature for this pixel derived from Eq. (3); and $T_r(x, y)$ denotes the fitted rural LST for this pixel derived from Eq. (1).

3.2.2. Selection of the SUHI estimators

For the estimation of next-day SUHIs, the controls that drive daily SUHI variations should be selected as estimators. As reported by Lai et al. (2021), the daily SUHI variations can be decomposed into two components: the *mid-term* and *day-to-day* SUHI variations, each with different categories of control. The decomposition of the SUHI variations can be generally expressed by Eq. (5); and an illustration of the complete

dynamics for the SUHI intensity over different scales is given in Fig. 2.

$$\lambda_d(t) = \underbrace{\lambda_a + \Delta\lambda_a(t)}_{\text{mid-term variation}} + \underbrace{\Delta\lambda_d(t)}_{\text{day-to-day variation}} = \lambda_{\text{mid}}(t) + \Delta\lambda_d(t) \quad (5)$$

where $\lambda_d(t)$ is the daily value of the chosen SUHI feature λ (i.e., I and T_G used in this study) on day t ; λ_a is the annual mean value of the SUHI feature; $\Delta\lambda_a$ and $\Delta\lambda_d$ are the intra-annual and day-to-day SUHI variations, respectively. λ_d , λ_{mid} (the combination of λ_a and $\Delta\lambda_a$), and λ_a represent the *short-*, *mid-*, and *long-term* SUHI dynamics respectively.

Two groups of factors that account for the *mid-term* SUHIs (λ_{mid}) and *day-to-day* SUHIs ($\Delta\lambda_d$) respectively should therefore be used as estimators. Ten factors were first selected based on the illustrated controls on these two components of the daily SUHIs (Chen et al., 2006; Lai et al., 2021; Lazzarini et al., 2013; Zhou et al., 2011). They include: the

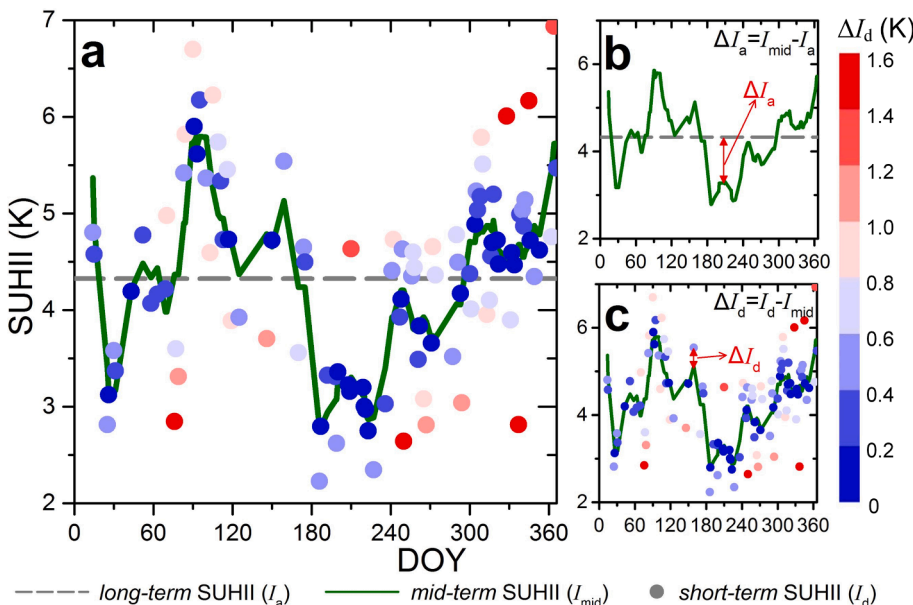


Fig. 2. SUHI intensity (I) dynamics on different time scales for the Xi'an city. Subplot a shows the SUHIs over the *long-term* scale (i.e., the annual mean SUHII, termed I_a , in dashed grey line), *mid-term* scale (i.e., the intra-annual SUHII, termed I_{mid} , in green line), and *short-term* scale (i.e., the observed daily SUHII, termed I_d , in dots with the dot color denoting the values of the day-to-day SUHII variations: ΔI_d). Here the *mid-term* SUHII (I_{mid}) was calculated as the mean I_d within the period of 10 days before and after the specified day (Lai et al., 2021). Subplots b and c illustrate the calculation of ΔI_{mid} and ΔI_d based on Eq (5), respectively. (For interpretation of the references to color in this figure legend, the reader is referred to the web version of this article.)

daytime length (*DL*), albedo (*ALB*), urban–rural contrast in NDVI ($NDVI_{u-r}$), rural surface temperature (T_r), relative humidity (*RH*), accumulated precipitation (*PREP*), surface air temperature (*SAT*), wind speed (*WDS*), rural diurnal temperature range (DTR_r), and aerosol optical depth (*AOD*). Among them, the former four factors are related to the *mid-term* SUHIs (Chen et al., 2006; Lai et al., 2021; Lazzarini et al., 2013; Zhou et al., 2011), whereas the latter six are related to the day-to-day SUHIs (Lai et al., 2021; Zhou et al., 2011). The variable *DL* was calculated following Göttsche and Olesen (2009); $NDVI_{u-r}$ was calculated as the difference between urban and rural averaged NDVI; the T_r and DTR_r were computed respectively as the mean surface temperature and mean diurnal temperature range across rural areas; while all the other variables were calculated as the mean values of all the available satellite observations or *in-situ* measurements (see Section 3.1 for the used dataset to calculate these variables) within the administrative boundary of each city.

To estimate the next-day SUHIs, the predicted next-day status of the chosen ten factors should be employed as estimators. For the factor *DL*, its next-day status (termed DL_{d+1}) can be directly calculated (Göttsche and Olesen, 2009). For the four primary meteorological variables (*RH*, *PREP*, *SAT* and *WDS*) with their next-day values being predicted well with numerical weather forecast system (Bauer et al., 2015), we directly employed their next-day measurements as estimators (respectively termed RH_{d+1} , $PREP_{d+1}$, SAT_{d+1} and WDS_{d+1}). We acknowledge that, under real estimation cases, the forecasting errors of these four variables do exist and they would reduce the estimation accuracy consequently. More discussions related to this issue are provided in Section 5.2. For all the other variables including *ALB*, $NDVI_{u-r}$, T_r , DTR_r , and *AOD* with their next-day values hard to obtain under real scenarios, we indirectly employed their preceding status as estimators: They were respectively termed ALB_{pre} , $NDVI_{u-r,pre}$, $T_{r,pre}$, $DTR_{r,pre}$, and AOD_{pre} , with the former two being calculated as the nearest available preceding observations while the latter three being calculated according to Eq. (2). The preceding status of the SUHI feature to be estimated (i.e., I_{pre} or $T_{G,pre}$ for estimation of the next-day *I* and T_G respectively) was used as the additional estimator considering its close relationships with the *mid-term* SUHIs. The preceding status I_{pre} (or $T_{G,pre}$) was calculated using the following equation:

$$\begin{cases} \beta_{pre}(t) = N^{-1} \sum_{k \in \Omega_{PRE}} \beta(k) \\ \Omega_{PRE} = \{t, t-1, t-2, \dots, t-9\} \end{cases} \quad (6)$$

where $\beta_{pre}(t)$ represents the preceding status of the variable β on day t ; $\beta(k)$ represents the value of variable β on day k , where k belongs to the *preceding period* of the specific day t (i.e., Ω_{PRE}); and N is the number of valid daily results during Ω_{PRE} . Note that the discussions in Section 5.3 demonstrate that by enlarging the distance between the *preceding period* (i.e., Ω_{PRE}) and the day to be estimated (i.e., the t), the estimation for the next-day SUHI can potentially be extended to the estimation of SUHIs for the next few days.

Finally, a total of 11 estimators were obtained, including the five estimators related to the *mid-term* SUHI component (λ_{mid}) and the six estimators related to the day-to-day SUHI components ($\Delta\lambda_d$). By combining these two groups of estimators, the statistical estimation of the next-day nighttime SUHIs can be performed using the following formula:

$$\begin{cases} \lambda_{d+1}(t) = \lambda_d(t+1) = \lambda_{mid}(t) + \Delta\lambda_d(t+1) = f(\beta_{mid}, \beta_{\Delta d}) \\ \beta_{mid} = \{DL_{d+1}, ALB_{pre}, NDVI_{u-r,pre}, T_{r,pre}, \lambda_{pre}\} \\ \beta_{\Delta d} = \{RH_{d+1}, PREP_{d+1}, SAT_{d+1}, WDS_{d+1}, DTR_{r,pre}, AOD_{pre}\} \end{cases} \quad (7)$$

where $\lambda_{d+1}(t)$ is the next-day value of SUHI feature λ (i.e., *I* and T_G) for day t ; λ_d , λ_{mid} , and $\Delta\lambda_d$ have the same meaning as in Eq. (5); β_{mid} and $\beta_{\Delta d}$ denote the two categories of SUHI estimators related to λ_{mid} and $\Delta\lambda_d$, respectively; $f(\cdot)$ represents the function between λ_d and SUHI

Table 2
Definitions of the input estimators for the next-day SUHI estimation.

Estimator name	Description	Data source	Group *
DL_{d+1}	next-day daytime length	calculation	β_{mid}
ALB_{pre}	preceding status of average albedo	MODIS	β_{mid}
$NDVI_{u-r,pre}$	preceding status of the urban–rural difference in NDVI	MODIS	β_{mid}
$T_{r,pre}$	preceding status of the rural mean LST	MODIS	β_{mid}
I_{pre}	preceding status of <i>I</i>	MODIS	β_{mid}
$T_{G,pre}$	preceding status of LST_G	MODIS	β_{mid}
RH_{d+1}	next-day average relative humidity	<i>in-situ</i> data	$\beta_{\Delta d}$
$PREP_{d+1}$	next-day average accumulated precipitation	<i>in-situ</i> data	$\beta_{\Delta d}$
SAT_{d+1}	next-day average surface air temperature	<i>in-situ</i> data	$\beta_{\Delta d}$
WDS_{d+1}	next-day average wind speed	<i>in-situ</i> data	$\beta_{\Delta d}$
$DTR_{r,pre}$	preceding status of the rural mean DTR	MODIS	$\beta_{\Delta d}$
AOD_{pre}	preceding status of the average AOD	MODIS	$\beta_{\Delta d}$

* ‘ β_{mid} ’ and ‘ $\beta_{\Delta d}$ ’ are the two categories of estimators related to *mid-term* and day-to-day SUHIs, respectively.

^a This estimator is only used for estimating the next-day SUHII (termed I_{d+1}).

^b This estimator is only used for estimating the next-day Gaussian-based LSTs (termed $T_{G,d+1}$).

estimators (i.e., β_{mid} and $\beta_{\Delta d}$); and the variable definitions contained in β_{mid} and $\beta_{\Delta d}$ are provided in Table 2. Note that for the pixel-based next-day Gaussian LST estimation (i.e., when the λ is T_G), all the estimators except the λ_{pre} have the same daily values across all the pixels within each city. Details on the derivation of $f(\cdot)$ are given in Section 3.2.3.

3.2.3. Implementation of the statistical estimation

To estimate statistically the next-day SUHIs with the estimators listed in Table 2, the function between the SUHIs and the associated estimators (i.e., $f(\cdot)$) given in Eq. (7) needs to be obtained first for each city. This study used an SVR model to derive the in-between function through an implicit style. The SVR is very efficient for modelling non-linear in-between relationships. It has a strong generalization ability and is very capable of avoiding overfitting by introducing slack variables which allow regression errors to exist (but penalizes the errors) (Durbha et al., 2007; Mountrakis et al., 2011; Vapnik, 1995). More importantly, it has been shown to outperform several other simple regression models and appropriate for nighttime SUHI modelling (Zhou et al., 2011).

Before training the SVR model in each single city, all of the input estimators listed in Table 2 were normalized to the range from 0 to 1 in order to eliminate the scaling effect of different magnitudes. The following equation was used:

$$\beta_{in} = (\beta_i - \beta_{min}) \cdot (\beta_{max} - \beta_{min})^{-1} \quad (8)$$

where β_{in} is the i -th value of the normalized variable set β ; β_i is the associated value before normalization; and β_{max} and β_{min} are respectively the maximum and minimum value of the variable set before normalization.

The radial basis function (RBF) was chosen as the kernel function, considering its reported high efficiency for modelling SUHIs (Zhou et al., 2011). Hyper-parameter C and kernel parameter γ of the RBF kernel are critical for the model performance (Hsu et al., 2010; Vapnik, 1995). We used the grid search technique and ten-fold cross-validation strategies to determine the best values of these two parameters among various

Table 3
Strategies for selecting validation and training samples.

SUHI feature	Validation sample	Training sample
I_{d+1}	randomly selected 20% of the samples	remaining 80% of the samples
$T_{G,d+1}$	patterns on one randomly selected day	patterns on the remaining days

possible combinations of them to avoid overfitting (Hsu et al., 2010). Specifically, for each combination of these two parameters, we cross-validated the model by dividing the training set into 10 subsets of equal size and repeated the model training and validation 10 times, with each subset as the testing samples whereas the remaining 9 as training samples. The average estimation accuracy of the cross-validation was calculated, and the best parameter values were finally determined, i.e., as the combination of parameter values with the highest estimation accuracy.

To evaluate the accuracy of the estimation strategy, some of the samples were used for training the SVR model while the rest were used for validation. For the next-day SUHII (I_{d+1}) estimation within each city, 20% of the daily results were randomly selected as validation samples (see Table 3). In order to eliminate possible biases induced by randomness, the estimation procedures were repeated five times within each city. For each of the five random samplings, the model performance was evaluated using the mean absolute error (MAE) and mean absolute percentage error (MAPE) between the estimated and reference results of the validation samples, and the final MAE/MAPE was calculated as the mean value of the five random samplings. For the next-day Gaussian-based LST ($T_{G,d+1}$) estimation, the LST image on one randomly selected day was used for validation each time. Model performance was then evaluated using the MAE between the estimated and reference LST images on that selected day.

3.2.4. Quantification of the factor contributions to SUHI estimation

In addition to the assessment of the overall performance of the SVR-based model, we further quantified the contributions from each or a specific group of estimators with reference to the overall estimation performance, using the model-independent permutation-based method (Genuer et al., 2010; Ho et al., 2014; Strobl et al., 2009). The contribution of each estimator was assessed using the following steps: (1) The SVR model was trained with the same training process as introduced in Section 3.2.3. (2) The values of this estimator in the validation samples were randomly permuted, and a new estimation was produced. (3) The contribution of this estimator was finally evaluated as the increase in the

MAE (as a percentage, termed MAE_{inc}) caused by the permutation. Note that permutation was repeated five times for each estimator, and the estimator contribution was calculated as the mean MAE_{inc} obtained from these five results.

In order to evaluate and then compare the combined contributions from the two groups of estimators (i.e., β_{mid} and $\beta_{\Delta d}$), further assessments were conducted. All of the associated assessment procedures were identical to those of individual estimators, except that permutations for a group of estimators, rather than for a single one, were made simultaneously each time.

The overall framework of this study is given in Fig. 3.

4. Results

4.1. Accuracy of the estimated SUHII

The performance of the proposed approach to estimate next-day nighttime SUHI is illustrated in Fig. 4. A high estimation accuracy was achieved, with a mean MAE of 0.67 K across the chosen cities, and the R^2 between the estimated and observed SUHI is 0.60. For more than 90% of these cities, the MAE is less than 1.0 K, and the MAPE is no more than 25%. Note that the MAE is relatively high (1.45 K) in one single city located within the NS zone (Fig. 4a). This poorer estimation performance is attributable to the relatively worse performance of the Gaussian modelling for the SUHI characterization over this specific city (discussions on the uncertainties of the Gaussian modelling are provided in Section 5.1).

The results further exhibit a latitudinal discrepancy in terms of the accuracy of the estimated SUHI, with the MAE generally larger in northern than in southern cities (Fig. 4a). Specifically, higher MAEs tend to occur for the cities located in the WT or eastern MT zone (the mean MAEs for cities in this two zones are 0.70 and 0.74 K respectively), while relatively lower errors occur for the cities in the MS and SS zones (the associated mean MAEs are 0.51 and 0.64 K for these two zones) (Fig. 5a). This spatial pattern of estimation performance was determined to be regulated by the day-to-day SUHI (i.e., ΔI_d): in cities where the SUHI

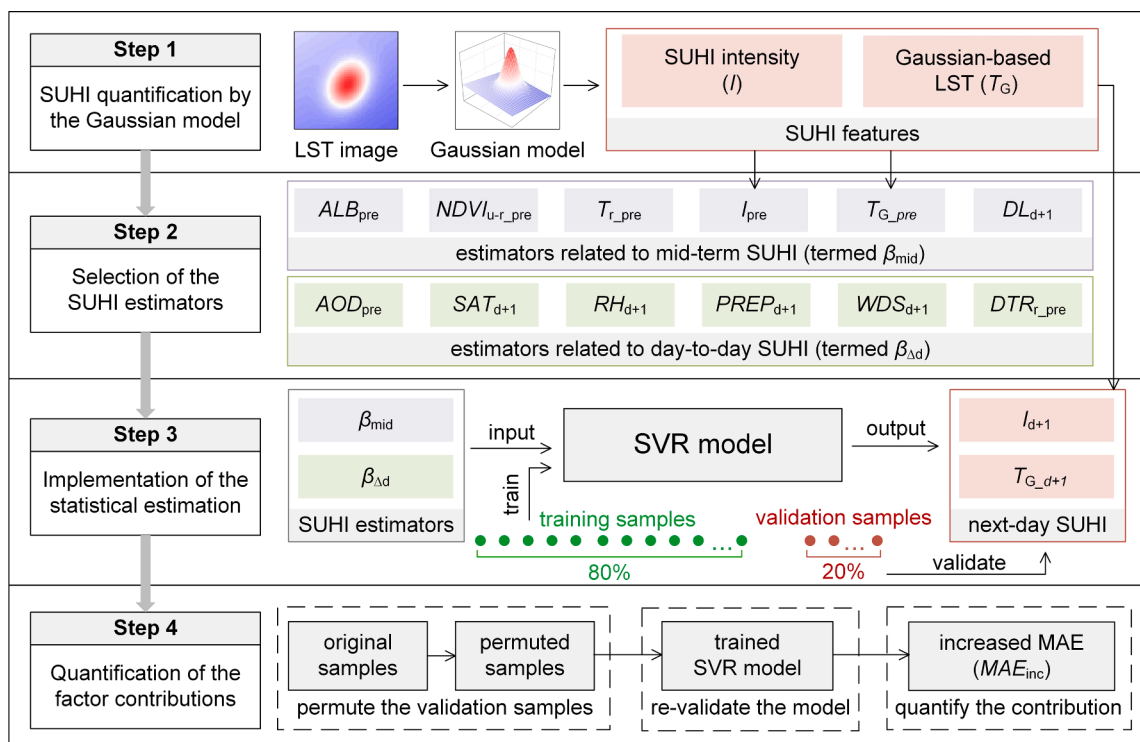


Fig. 3. Framework of this study. Definitions on the SUHI estimators in Step 2 were given in Table 2. More details for Steps 1–4 can be found in Sections 3.2.1–3.2.4.

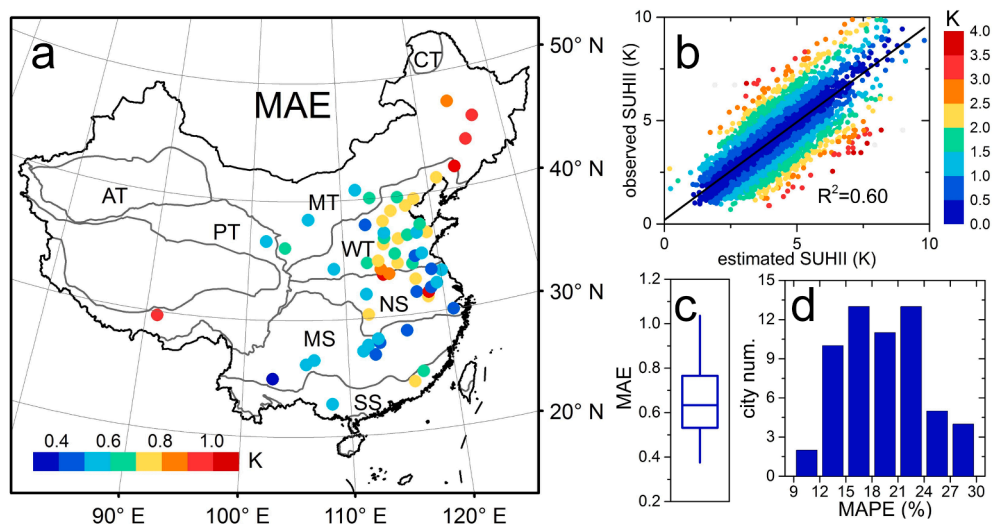


Fig. 4. Estimation performance of the next-day SUHIIs in the chosen cities. (a) shows the spatial distribution of the MAE (K). (b) provides the relationship between the estimated next-day SUHIIs and observed SUHIIs, with the dot colors representing the estimated absolute errors. (c) exhibits the boxplot for MAE. (d) displays the MAPE histogram, with the x- and y- axis denoting the MAPE (%) and city number respectively.

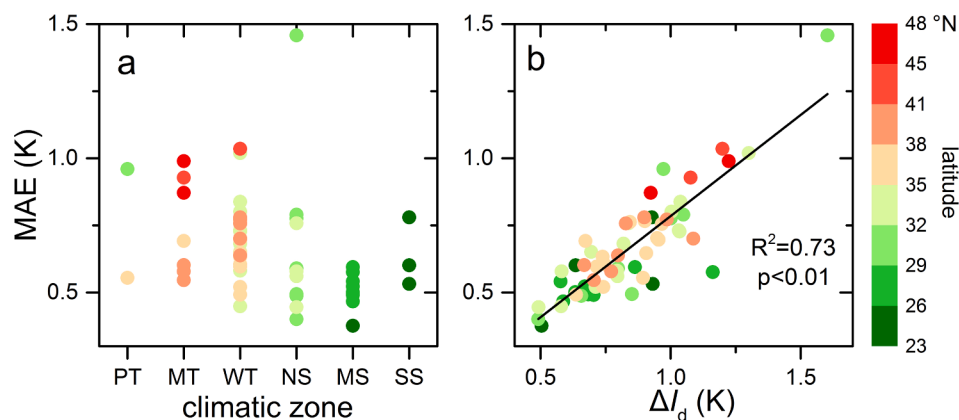


Fig. 5. Estimation performance (denoted by the MAE) of the next-day SUHIIs within different bioclimatic zones (a), and the relationship between the MAE and the annual mean absolute value of ΔI_d (b). Dot colors denote the latitude.

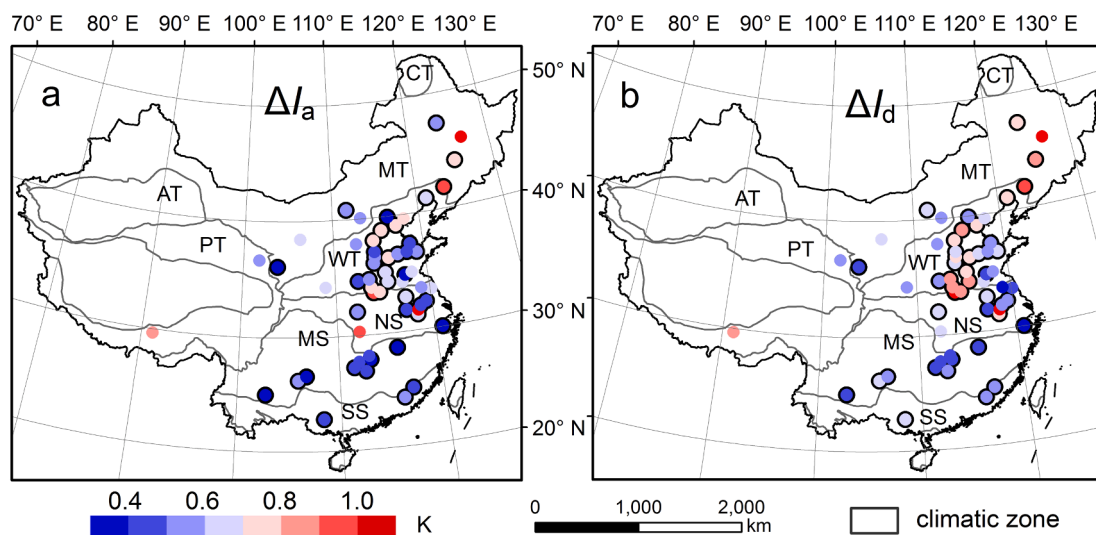


Fig. 6. Comparison of the annual mean absolute values of the intra-annual SUHII variations (ΔI_a , subplot a) and those of the day-to-day SUHII variations (ΔI_d , subplot b). The dots with a black boundary denote a higher annual mean absolute value for ΔI_d than that for ΔI_a .

shows a larger day-to-day fluctuation (with a larger annual absolute mean of ΔI_d , see Fig. 2 for the calculation of ΔI_d), the estimated MAE becomes higher (Fig. 5b). This indicates that the errors of the approach to estimating the next-day SUHIs come mainly from the estimation of their day-to-day components (ΔI_d) rather than from estimation of their *mid-term* components (I_{mid}). This phenomenon can be partly explained by the results shown in Fig. 6, which demonstrates that the day-to-day SUHIs generally have a larger variability than the *mid-term* SUHIs in most (>70%) cities, and consequently they are more difficult to estimate. In addition, previous studies have shown that day-to-day SUHIs (ΔI_d) are under a combined control of various factors (Lai et al., 2021; Quan, 2014; Zhou et al., 2011), and the selected estimators belonging to $\beta_{\Delta d}$ can only capture a portion of day-to-day SUHIs (ΔI_d). By comparison, the selected estimators belonging to β_{mid} are relatively more capable of representing *mid-term* SUHIs (I_{mid}) (Chen et al., 2006; Meng et al., 2018; Yao et al., 2017).

4.2. Accuracy of the estimated Gaussian-based LSTs

In addition, a pixel-by-pixel estimation for the next-day Gaussian-based LSTs ($T_{G,d+1}$) was achieved, and our assessments show that the estimated MAE is less than 2.0 K for nearly 80% of the cities. Detailed evaluations of the six megacities (see Fig. 1 for the locations) demonstrate that the proposed approach is capable of estimating the next-day LSTs with an acceptable accuracy (the MAE is less than 2.0 K) (Fig. 7). By incorporating various SUHI-related estimators, the preceding LSTs ($T_{G,pre}$) can be significantly adjusted to the next-day LSTs ($T_{G,d+1}$), with an adjustment up to 3 K (e.g., the MAE decreased by 3.4 and 3.3 K in Fig. 7b and d). To provide a detailed insight into the estimated pixel-by-pixel LSTs, we present the estimations for Xi'an on five randomly chosen days (see Fig. 8). Xi'an was chosen for the following reasons: (1) a satisfactory performance of the Gaussian modelling had been achieved for this city (the mean *RMSE* and *r* is 0.40 K and 0.88), and (2) the city is located in the WT zone where the daily SUHI variations are more strongly regulated by our selected SUHI estimators (Lai et al., 2021).

The comparisons shown in Fig. 8 support the competence of our approach in estimating next-day pixel-based LSTs. Specifically, the assessments indicate that the incorporated SUHI estimators can generally capture the high day-to-day LST fluctuations: the associated estimated MAEs are all less than 1.5 K, and the LST ranges of the estimated next-day images correspond well with those of the reference images (the

observed next-day images). These assessments also imply that the proposed approach is able to capture the spatial patterns of the LST images in most cases (Fig. 8): The Gaussian-based SUHI ellipses for the estimated LST images have similar shapes and orientations to those of the reference LST images on most days (e.g., on DOYs 111, 310, and 366). Note that the estimated SUHI ellipse may deviate from the reference one on a few days: e.g., the SUHI ellipse has a different orientation from the reference one on DOY 70. Such estimation biases may be caused by the inconsistency between the spatial resolution of pixel-by-pixel LST data and point-based *in-situ* measurements. In addition, both the estimated and reference next-day LST images in Fig. 8 should be spatially smoother than the true LSTs, as a result of the over-simplification of the Gaussian model; this issue is further discussed in Section 5.1.

4.3. Contributions of input estimators to SUHI estimation

The contributions of each estimator to the estimation of next-day SUHIs are shown in Fig. 9. The analysis demonstrates that RH_{d+1} is the most important estimator, and its permutation would cause an increase of 35% in the MAE on average (Fig. 9a). This greater importance of RH_{d+1} compared with other estimators corresponds well to its previously determined dominant control on daily SUHI variations (Quan, 2014; Zhou et al., 2011). Another two estimators related to day-to-day SUHIs, SAT_{d+1} , and WDS_{d+1} , also contribute greatly to the next-day SUHI estimation: permutations of these two estimators would increase the MAE by 14% and 8%, respectively. These previous three estimators, which are respectively related to surface thermal admittance, surface air temperature fluctuations, and atmospheric movement, are shown to significantly contribute to the next-day SUHI estimation. By comparison, the other three estimators, which also belong to $\beta_{\Delta d}$ (i.e., $DTR_{r,pre}$, AOD_{pre} , and $PREP_{d+1}$), make only a moderate contribution to the next-day SUHI estimation (all with MAE_{inc} less than 5%), despite the determined close relationships between these variables and the SUHI (Cao et al., 2016; Zhao et al., 2014; Zhou et al., 2011). We consider that the moderate contribution from $DTR_{r,pre}$ and AOD_{pre} to the SUHI estimation may result from the fact that we used their preceding status rather than their next-day values as estimators. The small contribution from $PREP_{d+1}$ can be explained by its high correlation with RH_{d+1} , as was also shown by Lai et al. (2021). In other words, the information loss by the permutation of $PREP_{d+1}$ is anticipated to be largely compensated by RH_{d+1} .

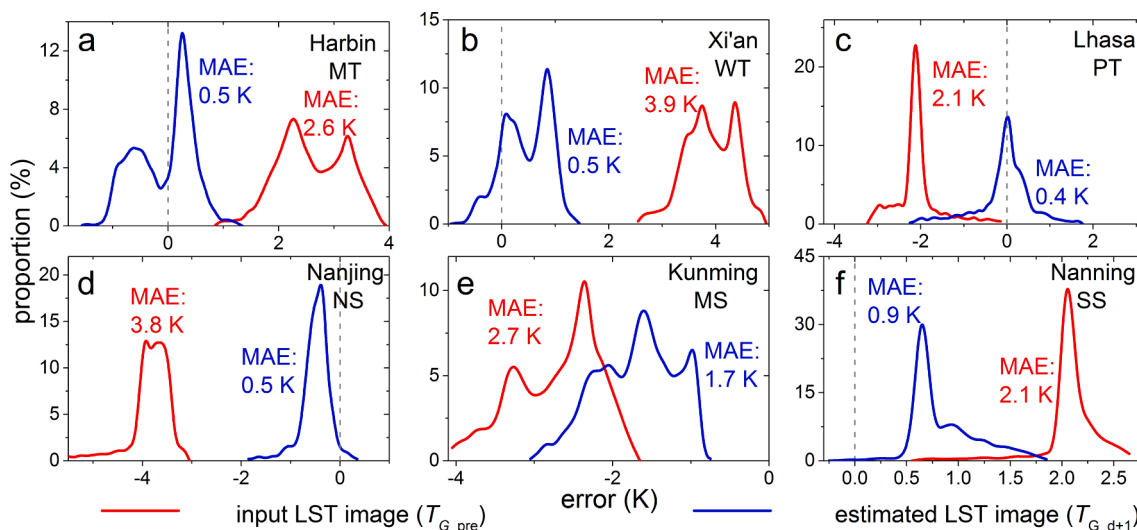


Fig. 7. Estimation accuracies for the Gaussian-based LSTs for the six megacities for one randomly selected day. The red lines denote the error histograms of the input preceding LSTs (the $T_{G,pre}$ images) referenced to the real next-day LST observations (the $T_{G,d+1}$ images), and the blue lines denote the error histograms of the estimated next-day LSTs (the estimated $T_{G,d+1}$ images) referenced to the real next-day LST observations. (For interpretation of the references to color in this figure legend, the reader is referred to the web version of this article.)

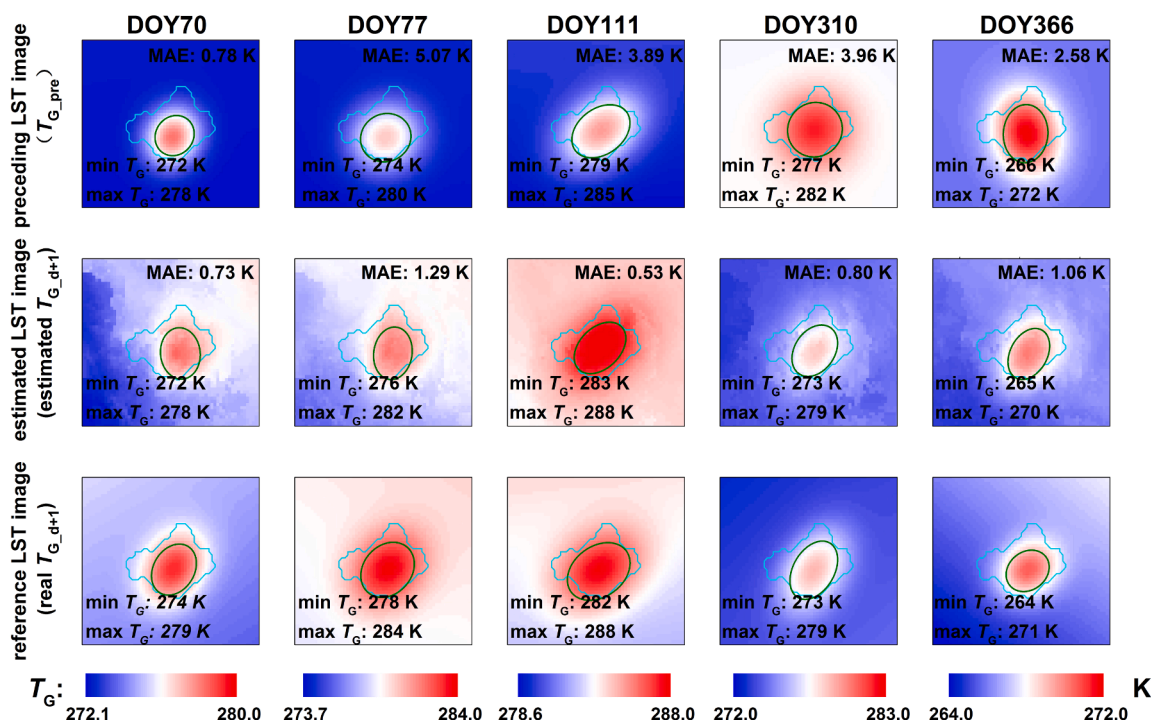


Fig. 8. Comparison of the input preceding LST (T_{G_pre}) images (the first row), the estimated next-day LST images (the estimated T_{G_d+1} image, the second row), and the reference LST images (the real T_{G_d+1} images, the third row) on five randomly selected days for Xi'an. The blue lines denote the boundary of urban areas (see Section 2 for the delineation of urban areas), and the green ellipses show the Gaussian-estimated SUHI ellipses (see Section 3.2.1 for derivation of the SUHI ellipse). (For interpretation of the references to color in this figure legend, the reader is referred to the web version of this article.)

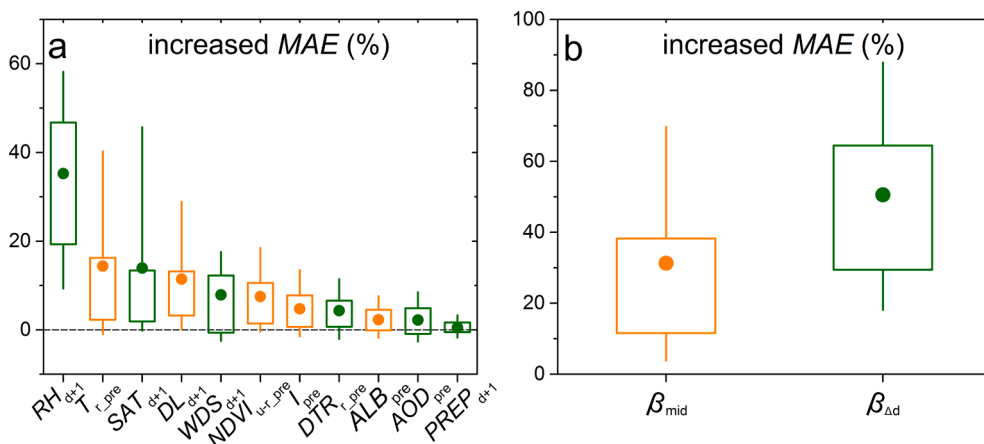


Fig. 9. Contribution of each single estimator (a) and those from the two groups of estimators (b) to the next-day SUHII estimation, represented by the increased MAE percentages (i.e., MAE_{inc} , unit: %) generated using the model-independent permutation analysis. The green boxes represent the contribution from estimators belonging to $\beta_{\Delta d}$, while the orange ones represent that from estimators belonging to β_{mid} . (For interpretation of the references to color in this figure legend, the reader is referred to the web version of this article.)

Among the estimators related to mid-term SUHI (β_{mid}), the contributions from T_{r_pre} and DL_{d+1} are the greatest, with an averaged MAE_{inc} of 14% and 11%. The highlighted effects of these two variable correspond well to the previously determined close relationships between them and the mid-term SUHIs (Zhou et al., 2011; Zhou et al., 2013). The contributions of the two estimators related to land cover type ($NDVI_{u-r_pre}$ and ALB_{pre}) are relatively lower (associated MAE_{inc} are 8% and 2%, respectively), despite their notable effects on mid-term SUHI variations (Lazzarini et al., 2013; Quan et al., 2014). Incorporation of the preceding status of the SUHII (I_{pre}) also contributes to the estimation, although the averaged MAE_{inc} is relatively low (5%). The relatively small contributions from these three estimators ($NDVI_{u-r_pre}$, ALB_{pre} , and I_{pre}) likely result from their dependence on the estimator DL_{d+1} (a substitute for solar radiation and surface phenology).

Although the contribution of each individual estimator appears to be not especially high (i.e., the associated MAE_{inc} are all less than 15%,

except for RH_{d+1}), we nevertheless emphasize that their combined contributions are substantial. Specifically, the mean MAE_{inc} induced by the permutation of β_{mid} (estimators related to mid-term SUHIs) is 31%, and that for $\beta_{\Delta d}$ (estimators related to day-to-day SUHIs) is 51% (Fig. 9b). Further analysis suggests that, for nearly 78% of the cities, a higher contribution from $\beta_{\Delta d}$ than β_{mid} is observed (Fig. 10). Such a contrast can be partly explained by the fact that the daily SUHII is expressed more by its day-to-day dynamics than by its mid-term variations (i.e., a larger ΔI_d than ΔI_a is shown for most cities (Fig. 6)). In other words, an accurate estimation of ΔI_d can capture more of the actual changes in the daily SUHIs, and therefore it contributes more to the next-day SUHII estimation. The higher contributions of some estimators belonging to $\beta_{\Delta d}$ may also result from their capacity to explain not only the day-to-day but also the mid-term components of the SUHIs: the monthly/seasonal SUHIs have been determined to be partly regulated by monthly/seasonal changes in some meteorological variables (e.g., RH ,

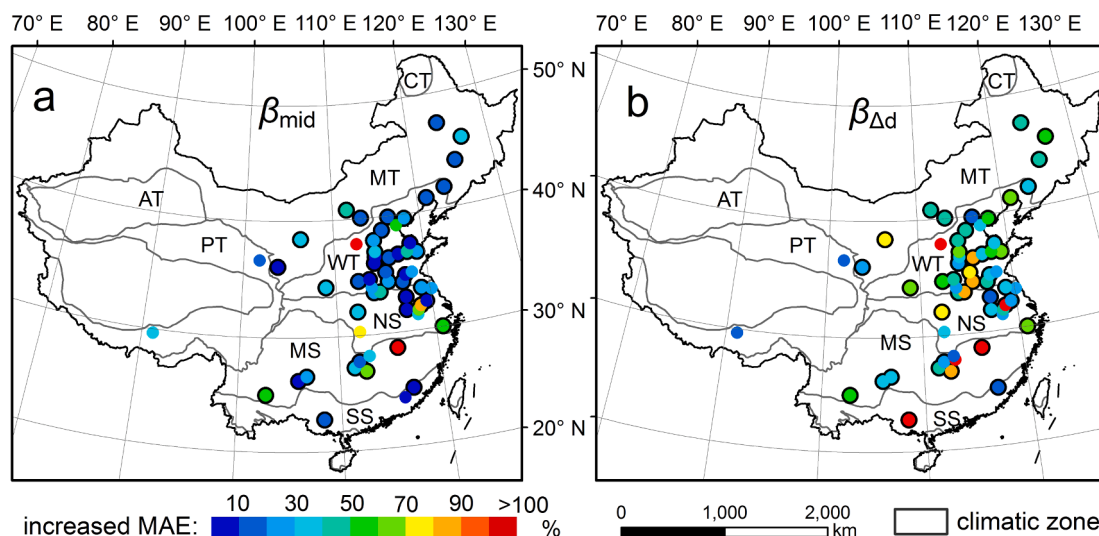


Fig. 10. Comparison of the contributions of the estimators related to mid-term SUHIs (β_{mid} , subplot a) and those related to day-to-day SUHIs ($\beta_{\Delta d}$, subplot b) to the next-day SUHII estimation, represented by increased MAE percentages (unit: %). The dots with a black boundary indicate that the contribution from $\beta_{\Delta d}$ is higher than that from β_{mid} in the associated city.

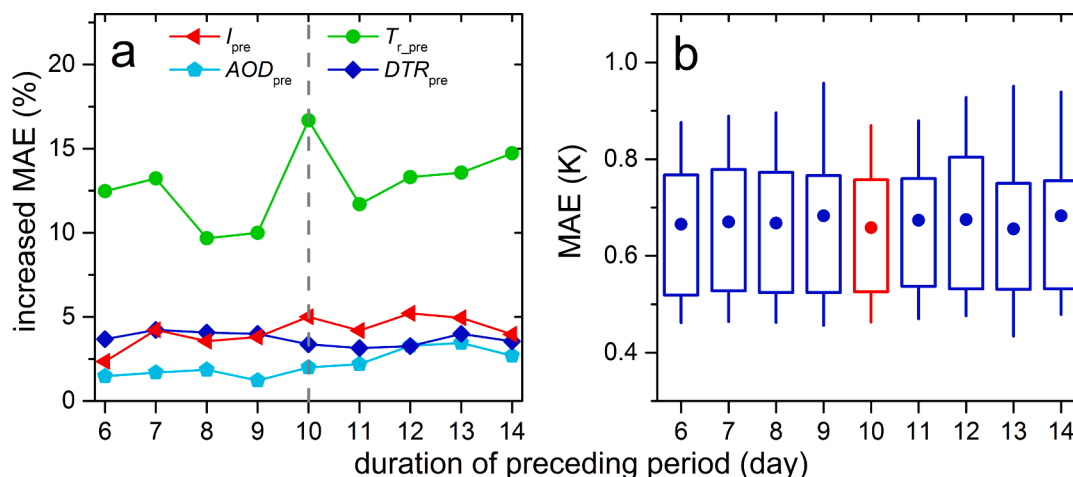


Fig. 11. Results of sensitivity analysis of the SUHII estimation with reference to the definition of the *preceding period*. The results are represented by changes in the increased MAE percentage for each estimator (a) and by the changes of the estimated MAE (b), along with the changes in the duration of the *preceding period* (the range from 5 to 15 days). The red boxplot in (b) represents the estimation performance in this study (i.e., the duration was set to 10 days). (For interpretation of the references to color in this figure legend, the reader is referred to the web version of this article.)

SAT, and PREP) (Du et al., 2016; Zhou et al., 2016).

4.4. Sensitivity analysis of the duration of the preceding period

For the SUHI estimation, this study has employed various estimators (i.e., ALB_{pre} , $NDVI_{u-r,pre}$, I_{pre} , $T_{r,pre}$, $DTR_{r,pre}$, and AOD_{pre}) for which the mean values during the *preceding period* were calculated to help the estimation (see Eq. (6)). Arguably, different definitions of the *preceding period* would introduce uncertainties into the estimation. A sensitivity analysis was therefore conducted to investigate the impacts from the duration of the *preceding period* in terms of the contributions from the four estimators (including I_{pre} , $T_{r,pre}$, $DTR_{r,pre}$, and AOD_{pre}) on the SUHII estimations (see Fig. 11a) as well as on the SUHII estimation performance (see Fig. 11b). Here we did not analyze the impacts from *preceding period* duration in terms of the contributions from ALB_{pre} and $NDVI_{u-r,pre}$ because these two estimators possess a relatively lower temporal variability and would therefore remain insensitive to the *preceding period* duration.

The results show that this duration, although does influence the

contributions of some estimators (e.g., $T_{r,pre}$, Fig. 11a), would not substantially distort the estimation performance: the mean MAE remains stable along with the duration change (Fig. 11b). One reason for such a low degree of sensitivity is that the combined contributions from the remaining estimators (i.e., RH_{d+1} , WDS_{d+1} , $PREP_{d+1}$, SAT_{d+1} , and SH_{d+1}) have already captured a large portion of the daily SUHII variations (see Fig. 9).

5. Discussion

Characterization and modelling of the temporal variations of the SUHIs are critical for improving our understanding of the urban thermal environment. Insights have been provided on SUHI dynamics on various time scales (Chakraborty et al., 2017; Lai et al., 2018; Meng et al., 2018; Quan et al., 2014; Yang et al., 2019; Zhou et al., 2019). These studies, however, are mainly restricted to the analysis of past (or elapsed) SUHI dynamics. A recent study further endeavored to offer a nowcasting (a real-time estimation) of the urban thermal environment (Keramitsoglou et al., 2016). Our study has made further progress through the

estimation of next-day SUHIs. In addition, the estimated pixel-by-pixel next-day LSTs, when combined with forecasted meteorological conditions (e.g., relative humidity, SAT, and wind speed), is able to generate a next-day map of human thermal comfort (Ge et al., 2017).

This study has mainly adopted a statistical approach to estimating SUHIs. Its statistical nature endows it with simplicity (low computational complexity) and efficiency in estimation; and in addition its generalizability has been demonstrated by the incorporation of the SVR to obtain the statistical relationships between the SUHIs and their associated estimators (Mathew et al., 2019; Quan, 2014; Zhou et al., 2011). Further, the reported statistically close relationship between the SUHIs and estimators lays the foundation for the design of diagnostic equations for more accurately estimating daily nighttime SUHIs, as already proposed for CUHIs (Theeuwes et al., 2017; Zhang et al., 2019). We nevertheless need to emphasize that the statistical approach does not invalidate - and therefore is not intended to replace - numerical weather forecasting (e.g., those based on the Weather Research and Forecasting Model), which possesses much greater flexibility for SUHI estimations/predictions in more complex scenarios and environments (Li and Bou-Zeid, 2014; Zhao et al., 2018). In the following section, we discuss several additional issues regarding the uncertainties and prospects of this study.

5.1. Uncertainties related to the Gaussian-quantified SUHIs

With the assistance of the SVR model and various estimators related to the daily SUHI variations, we proposed a statistical approach for estimating the next-day nighttime SUHIs. The performance of the proposed approach was evaluated by the indicators that measure the magnitude and spatial patterns of the SUHI respectively (i.e., the SUHI and pixel-by-pixel LSTs), which were both obtained through the Gaussian model. Despite the frequent use of the Gaussian model to quantify the SUHI intensity as well as its capability for overall characterization of SUHIs (Anniballe and Bonafoni, 2015; Quan et al., 2014; Tran et al., 2006; Zhou et al., 2011), additional errors may still be induced by this model (Lai et al., 2021). Although such errors can be largely suppressed by the strict selection of daily samples based on the performance of Gaussian model, distortions may remain for some cities (see Section 3.2.1). For example, in cities with thermal landscape that does not follow the Gaussian distribution, the Gaussian model may become less appropriate for the SUHI intensity quantification. For such cities, we can use other indicators to quantify the SUHI intensity (Schwarz et al., 2011; Bechtel et al., 2019), such as the mean LST difference between the urban surface and rural buffer (Voogt and Oke, 2003), the difference between the maximum and mean of LST (Rajasekar and Weng, 2009), or the LST difference between the urban area and cropland (Jin, 2005). It is anticipated that even with a different SUHI indicator, its next-day value can as well be estimated using the proposed approach by combining the chosen SUHI-related estimators and an SVR model.

The Gaussian model also has deficiencies in estimating LST patterns, despite its relatively low sensitivity to cloud cover. The Gaussian-based LSTs (T_G), which were designed from the perspective of global characterization, can only represent the overall spatial variations of the SUHIs. As a result, the exhibited Gaussian-based next-day LSTs (see Fig. 8) are of only global significance, and they are less capable of representing the local LST variations with occasional high heterogeneity. Solutions to these issues require the design of an enhanced model that is more sensitive to both the overall and local SUHI features. Over cities with very few clouds, one compromise solution can be the direct use of the original LSTs, in which case the Gaussian model is unnecessary.

5.2. Uncertainties related to SUHI estimators

Different categories of factors have been reported as controls of SUHI variations on different timescales, as discussed in the Introduction. This study chose a series factors as estimators for the next-day nighttime SUHI estimations, based on previous investigations of the controls on daily nighttime SUHI variations (Lai et al., 2021; Quan, 2014; Zhou et al., 2011). A generally high estimation accuracy was achieved, assisted by the close relationship between these estimators and SUHIs, as well as the four estimators (i.e., *RH*, *PREP*, *WDS*, and *SAT*) that are predictable by numerical weather forecast system. Uncertainties related to the estimators however exist, mainly in the following two aspects.

First, for these four meteorological variables (including *RH*, *PREP*, *WDS*, and *SAT*), we directly used their next-day measurements in substitute for their forecasted values as estimators. Although such a substitute should be reasonable in most cases in consideration of the increasing reliability of weather forecasting results in recent years (Bauer et al., 2015), uncertainties in terms of the weather forecasting errors do exist, and may therefore decrease the estimation accuracy of the next-day SUHIs. To quantify the impacts of such uncertainties on the proposed approach, we conducted a sensitive analysis that complied with the following three steps: (1) for each of these four variables, 8 groups of random errors were generated whose absolute values account for 0 ~ 5%, 5 ~ 10%, 10 ~ 15%, 15 ~ 20%, 20 ~ 25%, 25 ~ 30%, 30 ~ 35%, and 35 ~ 40% of the real daily measurements; (2) new estimators with an MAPE ranging from 0 to 40% were derived for each variable, by adding each group of errors with the corresponding measurements; (3) by replacing the original estimators (with an MAPE of 0%) with the new ones and re-conducting the estimation, the impacts from the forecasting errors of these four variables were assessed using the increased MAEs in the estimated next-day SUHIs (see Fig. 12).

Second, although the estimators incorporated in this study have successfully supported the estimation (Section 4.3), they are still unable to capture fully the daily SUHI variations. Future attempts to improve the accuracy of SUHI estimation should consider the integration of more estimators, especially those related to *short-term* SUHI variations. For example, the variables related to anthropogenic heat (AH) release are anticipated to contribute to SUHI estimation, because AH changes the surface energy balance and therefore affects the urban thermal environment, especially at night (Kato and Yamaguchi, 2005). It would also be helpful if daily measurements related to radiation (including both short-wave/long-wave radiation) are incorporated as estimators, because the LST, when compared to the SAT, is more responsive to radiation (Oke et al., 2017).

5.3. Applications of the approach to SUHI estimations under other scenarios

The proposed approach is found to be efficient in estimating next-day nighttime SUHI intensity and pixel-by-pixel LSTs under clear-sky. Moreover, the approach has the potential for SUHI estimation under scenarios far beyond this restricted case, and we provide some examples below. First, the strategy can be applied to estimate SUHIs under all-weather conditions, if cloud coverage is incorporated as one of the input estimators, and the LSTs under clouds are reconstructed using a specific method (Fan et al., 2015). Second, the approach can be used to estimate SUHIs for daytime, once the issue of strong daytime thermal anisotropy is addressed by adjusting the slant observations into the nadir with a correction algorithm (Hu et al., 2016; Voogt, 2008). Third, with hourly or sub-hourly geostationary satellite thermal data, the estimation of next-day SUHIs can be extended from an instantaneous time into a full diurnal cycle. Forth, the assessments in Fig. 13 show that the

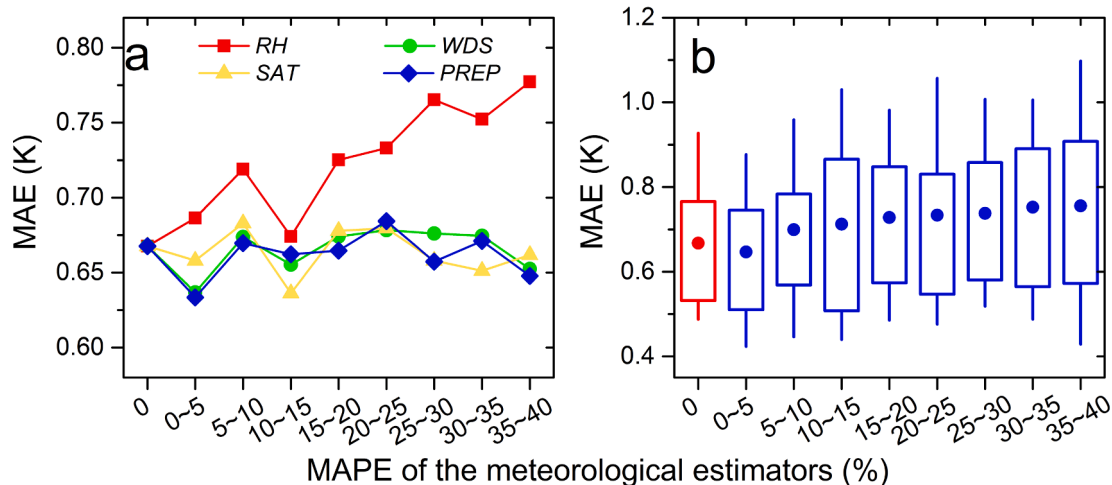


Fig. 12. Sensitivity analysis of the next-day SUHII estimation with regard to the forecasting errors of the four meteorological variables (i.e., the *RH*, *PREP*, *WDS*, and *SAT*). The sensitivity was represented with (a) the changes in the mean MAE (K) by changing the MAPE (%) of the four estimators individually, and with (b) the MAE boxplots by changing simultaneously the MAPE (%) of all the four estimators.

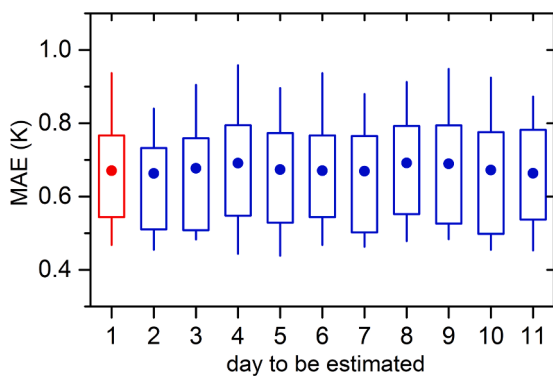


Fig. 13. Performance comparison (denoted by the MAE, unit: K) for estimating the next-day SUHII (the red boxplot) and the SUHIIs in several days (ranging from two to eleven - the blue boxplots). (For interpretation of the references to color in this figure legend, the reader is referred to the web version of this article.)

performance of the approach is generally good for longer periods (longer than the next-day), on condition that the forecasted weather conditions are sufficiently accurate (the sensitivity analysis of the estimation accuracy to the weather forecasting errors is provided in Section 5.2). This demonstrated robustness indicates that, using a comparable approach, the SUHIs in decades can be potentially better predicted by combining the climate-model-projected future climate conditions (including *RH*, *WDS*, *PREP*, and *SAT*) and projected future urbanization processes (Firozjaei et al., 2018; Mushore et al., 2017; Tran et al., 2017).

6. Conclusion

The estimation of SUHI dynamics on multiple time scales is a major focus of efforts to improve understanding of the urban surface climate. Most previous studies have modelled the SUHI variations for past periods, whereas estimation for future SUHIs, especially at the daily (i.e., day-to-day) scale, is rarely investigated. To address this gap, the present study incorporates both meteorological and surface controls to estimate next-day nighttime SUHIs, using an SVR model.

The results show that the proposed approach performs well in estimating both SUHI intensity (SUHII) and the pixel-by-pixel Gaussian-based LSTs. The mean MAE of the estimated SUHII is 0.67 K across the chosen Chinese cities, and the MAPE is no more than 25% for more than 90% of the cities. For the Gaussian-based LSTs, the estimated MAEs are mostly less than 2.0 K. Further assessment shows that, for nearly 78% of the chosen cities, the combined contributions from estimators related to day-to-day SUHIs ($\beta_{\Delta d}$) are greater than estimators related to *mid-term* SUHIs (β_{mid}), with associated mean MAE_{inc} of 51% and 31%, respectively. Among all the SUHI estimators, the contribution from RH_{d+1} is the largest, whose permutation can generate an estimated MAE increase (i.e., MAE_{inc}) of 35%. The contributions from the other two estimators related to day-to-day SUHIs (i.e., SAT_{d+1} , and WDS_{d+1}) are also relevant, with the associated mean MAE_{inc} reaching 14% and 8%, respectively.

We acknowledge that some uncertainties exist in terms of the Gaussian modelling and SUHI estimators, which may limit estimation accuracy. Nevertheless, by providing a feasible yet simple approach for estimating next-day nighttime SUHIs, this study fills a knowledge gap in the SUHI estimation and is consequently helpful for supporting adaptation to and mitigation of SUHI.

Declaration of Competing Interest

The authors declare that they have no known competing financial interests or personal relationships that could have appeared to influence the work reported in this paper.

Acknowledgments

We are grateful to all of the organizations/institutions from which the datasets were freely obtained. The MODIS data were downloaded from NASA’s Earth Observing System and Data and Information System (EOSDIS) (<https://earthdata.nasa.gov/>).

This work is supported jointly by the National Key R&D Program of China (Grant number: 2017YFA0603604), the Fundamental Research Funds for the Central Universities (Grant number: 090414380024), Jiangsu Provincial Natural Science Foundation (Grant number: BK20180009), the National Natural Science Foundation of China (Grant number: 41671420), and the Jiangsu Provincial Graduate Student Innovation Project (Grant number: KYCX19_0036). We are also grateful

for the financial support provided by the National Youth Talent Support Program of China.

References

- Ahmed, B., Kamruzzaman, M., Zhu, X., Rahman, M.S., Choi, K., 2013. Simulating land cover changes and their impacts on land surface temperature in Dhaka, Bangladesh. *Remote Sens.* 5 (11), 5969–5998.
- Anniballe, R., Bonafoni, S., 2015. A stable Gaussian fitting procedure for the parameterization of remote sensed thermal images. *Algorithms* 8 (2), 82–91.
- Bauer, P., Thorpe, A., Brunet, G., 2015. The quiet revolution of numerical weather prediction. *Nature* 525 (7567), 47–55.
- Bechtel, B., 2015. A new global climatology of annual land surface temperature. *Remote Sens.* 7 (3), 2850–2870. <https://doi.org/10.3390/rs70302850>.
- Bechtel, B., Demuzere, M., Mills, G., Zhan, W., Sismanidis, P., Small, C., Voogt, J., 2019. SUHI analysis using Local Climate Zones—A comparison of 50 cities. *Urban Clim.* 28, 100451. <https://doi.org/10.1016/j.uclim.2019.01.005>.
- Cao, C., Lee, X., Liu, S., Schultz, N., Xiao, W., Zhang, M., Zhao, L., 2016. Urban heat islands in China enhanced by haze pollution. *Nature Commun.* 7, 12509. <https://doi.org/10.1038/ncomms12509>.
- Chakraborty, T., Sarangi, C., Tripathi, S.N., 2017. Understanding diurnality and inter-seasonality of a sub-tropical urban heat island. *Bound-Lay. Meteorol.* 163 (2), 287–309.
- Chakraborty, T., Lee, X., 2019. A simplified urban-extent algorithm to characterize surface urban heat islands on a global scale and examine vegetation control on their spatiotemporal variability. *Int. J. Appl. Earth Obs.* 74, 269–280.
- Chakraborty, T., Hsu, A., Many, D., Sherif, G., 2020. A spatially explicit surface urban heat island database for the United States: Characterization, uncertainties, and possible applications. *ISPRS J. Photogramm.* 168, 74–88.
- Chen, X.L., Zhao, H.M., Li, P.X., Yin, Z.Y., 2006. Remote sensing image-based analysis of the relationship between urban heat island and land use/cover changes. *Remote Sens. Environ.* 104 (2), 133–146.
- Clinton, N., Gong, P., 2013. MODIS detected surface urban heat islands and sinks: Global locations and controls. *Remote Sens. Environ.* 134 (5), 294–304. <https://doi.org/10.1016/j.rse.2013.03.008>.
- Du, H., Wang, D., Wang, Y., Zhao, X., Qin, F., Jiang, H., Cai, Y., 2016. Influences of land cover types, meteorological conditions, anthropogenic heat and urban area on surface urban heat island in the Yangtze River Delta Urban Agglomeration. *Sci. Total Environ.* 571, 461–470.
- Durbha, S.S., King, R.L., Younan, N.H., 2007. Support vector machines regression for retrieval of leaf area index from multiangle imaging spectroradiometer. *Remote Sens. Environ.* 107, 348–361.
- Fan, X., Tang, B., Wu, H., Yan, G., Li, Z., 2015. A three-channel algorithm for retrieving night-time land surface temperature from MODIS data under thin cirrus clouds. *Int. J. Remote Sens.* 36 (19–20), 4836–4863.
- Feng, J., Cai, X., Chapman, L., 2019. Impact of atmospheric conditions and levels of urbanisation on the relationship between nocturnal surface and urban canopy heat islands. *Q. J. Roy. Meteor. Soc.* <https://doi.org/10.1002/qj.3619>.
- Feng, X., Myint, S.W., 2016. Exploring the effect of neighboring land cover pattern on land surface temperature of central building objects. *Build. Environ.* 95, 346–354.
- Firozjahi, M.K., Kiavarz, M., Alavipanah, S.K., Lakes, T., Qureshi, S., 2018. Monitoring and forecasting heat island intensity through multi-temporal image analysis and cellular automata-Markov chain modelling: A case of Babol city. *Iran. Ecol. Indic.* 91, 155–170.
- Fu, P., Weng, Q., 2016. A time series analysis of urbanization induced land use and land cover change and its impact on land surface temperature with Landsat imagery. *Remote Sens. Environ.* 175, 205–214.
- Fu, P., Weng, Q., 2018. Variability in annual temperature cycle in the urban areas of the United States as revealed by MODIS imagery. *ISPRS J. Photogramm.* 146, 65–73.
- Ge, Q., Kong, Q., Xi, J., Zheng, J., 2017. Application of UTCI in China from tourism perspective. *Theor. Appl. Climatol.* 128 (3–4), 551–561.
- Genuer, R., Poggi, J.M., Tuleau-Malot, C., 2010. Variable selection using random forests. *Pattern Recogn. Lett.* 31 (14), 2225–2236.
- Gong, P., Liang, S., Carlton, E.J., Jiang, Q., Wu, J., Wang, L., Remais, J.V., 2012. Urbanisation and health in China. *Lancet* 379 (9818), 843–852. [https://doi.org/10.1016/S0140-6736\(11\)61878-3](https://doi.org/10.1016/S0140-6736(11)61878-3).
- Göttsche, F.M., Olesen, F.S., 2009. Modelling the effect of optical thickness on diurnal cycles of land surface temperature. *Remote Sens. Environ.* 113 (11), 2306–2316.
- Grimm, N.B., Faeth, S.H., Golubiewski, N.E., Redman, C.L., Wu, J., Bai, X., Briggs, J.M., 2008. Global change and the ecology of cities. *Science* 319 (5864), 756–760. <https://doi.org/10.1126/science.1150195>.
- Ho, H.C., Knudby, A., Sirovyak, P., Xu, Y., Hodul, M., Henderson, S.B., 2014. Mapping maximum urban air temperature on hot summer days. *Remote Sens. Environ.* 154, 38–45.
- Hsu, C.W., Chang, C.C., Lin, C.J., 2010. A practical guide to support vector classification. [Online]. Available: <http://www.csie.ntu.edu.tw/~cjlin/>.
- Hu, L., Brunzell, N.A., 2015. A new perspective to assess the urban heat island through remotely sensed atmospheric profiles. *Remote Sens. Environ.* 158, 393–406. <https://doi.org/10.1016/j.rse.2014.10.022>.
- Hu, L., Monaghan, A., Voogt, J.A., Barlage, M., 2016. A first satellite-based observational assessment of urban thermal anisotropy. *Remote Sens. Environ.* 181, 111–121. <https://doi.org/10.1016/j.rse.2016.03.043>.
- Huang, X., Wang, Y., 2019. Investigating the effects of 3D urban morphology on the surface urban heat island effect in urban functional zones by using high-resolution remote sensing data: A case study of Wuhan, Central China. *ISPRS J. Photogramm.* 152, 119–131.
- Huang, Y., Yuan, M., Lu, Y., 2019. Spatially varying relationships between surface urban heat islands and driving factors across cities in China. *Environ. Plan. B-Urban* 46 (2), 377–394.
- Imhoff, M.L., Zhang, P., Wolfe, R.E., Bounoua, L., 2010. Remote sensing of the urban heat island effect across biomes in the continental USA. *Remote Sens. Environ.* 114 (3), 504–513. <https://doi.org/10.1016/j.rse.2009.10.008>.
- Kato, S., Yamaguchi, Y., 2005. Analysis of urban heat-island effect using ASTER and ETM + Data: Separation of anthropogenic heat discharge and natural heat radiation from sensible heat flux. *Remote Sens. Environ.* 99 (1–2), 44–54.
- Keramitsoglou, I., Kiranoudis, C.T., Ceriola, G., Weng, Q., Rajasekar, U., 2011. Identification and analysis of urban surface temperature patterns in Greater Athens, Greece, using MODIS imagery. *Remote Sens. Environ.* 115 (12), 3080–3090. <https://doi.org/10.1016/j.rse.2011.06.014>.
- Keramitsoglou, I., Kiranoudis, C., Sismanidis, P., Zakšek, K., 2016. An online system for nowcasting satellite derived temperatures for urban areas. *Remote Sens.* 8 (4), 306. <https://doi.org/10.3390/rs8040306>.
- Knapp, S., Kühn, I., Stolle, J., Klotz, S., 2010. Changes in the functional composition of a Central European urban flora over three centuries. *Perspect. Plant Ecol.* 12 (3), 235–244. <https://doi.org/10.1016/j.ppees.2009.11.001>.
- Lai, J., Zhan, W., Huang, F., Voogt, J., Bechtel, B., Allen, M., Peng, S., Hong, F., Liu, Y., Du, P., 2018. Identification of typical diurnal patterns for clear-sky climatology of surface urban heat islands. *Remote Sens. Environ.* 217, 203–220.
- Lai, J., Zhan, W., Voogt, J., Quan, J., Huang, F., Zhou, J., Bechtel, B., Hu, L., Wang, K., Cao, C., Lee, X., 2021. Meteorological controls on daily variations of nighttime surface urban heat islands. *Remote Sens. Environ.* 253, 112198. <https://doi.org/10.1016/j.rse.2020.112198>.
- Lazzarini, M., Marpu, P.R., Ghedira, H., 2013. Temperature-land cover interactions: The inversion of urban heat island phenomenon in desert city areas. *Remote Sens. Environ.* 130 (4), 136–152.
- Lee, Y., Kim, J., Yun, G., 2016. The neural network predictive model for heat island intensity in Seoul. *Energy Buildings* 110, 353–361.
- Li, D., Bou-Zeid, E., 2014. Quality and sensitivity of high-resolution numerical simulation of urban heat islands. *Environ. Res. Lett.* 9(5), 055001.
- Li, Y., Wang, L., Liu, M., Zhao, G., He, T., Mao, Q., 2019. Associated determinants of surface urban heat islands across 1449 cities in China. *Adv. Meteorol.* 2019, 4892714. <https://doi.org/10.1155/2019/4892714>.
- Liao, W., Liu, X., Wang, D., Sheng, Y., 2017. The impact of energy consumption on the surface urban heat island in China's 32 major cities. *Remote Sens.* 9 (3), 250. <https://doi.org/10.3390/rs9030250>.
- Lin, Y., Jim, C.Y., Deng, J., Wang, Z., 2018. Urbanization effect on spatiotemporal thermal patterns and changes in Hangzhou (China). *Build. Environ.* 145, 166–176.
- Maimaitiyming, M., Ghulam, A., Tiyyip, T., Pla, F., Latorre-Carmona, P., Halik, Ü., Sawut, M., Caetano, M., 2014. Effects of green space spatial pattern on land surface temperature: Implications for sustainable urban planning and climate change adaptation. *ISPRS J. Photogramm.* 89, 59–66.
- Mathew, A., Sreekumar, S., Khandelwal, S., Kumar, R., 2019. Prediction of land surface temperatures for surface urban heat island assessment over Chandigarh city using support vector regression model. *Sol. Energy* 186, 404–415.
- Meng, Q., Zhang, L., Sun, Z., Meng, F., Wang, L., Sun, Y., 2018. Characterizing spatial and temporal trends of surface urban heat island effect in an urban main built-up area: a 12-year case study in Beijing, China. *Remote Sens. Environ.* 204, 826–837. <https://doi.org/10.1016/j.rse.2017.09.019>.
- Mountrakis, G., Im, J., Ogole, C., 2011. Support vector machines in remote sensing: A review. *ISPRS J. Photogramm. Remote Sens.* 66 (3), 247–259.
- Mushore, T.D., Odindi, J., Dube, T., Mutanga, O., 2017. Prediction of future urban surface temperatures using medium resolution satellite data in Harare metropolitan city, Zimbabwe. *Build. Environ.* 122 (2017), 397–410.
- Nichol, J., 2009. An emissivity modulation method for spatial enhancement of thermal satellite images in urban heat island analysis. *Photogramm. Eng. Rem. S.* 75 (5), 547–556.
- Nichol, J.E., Fung, W.Y., Lam, K.S., Wong, M.S., 2009. Urban heat island diagnosis using ASTER satellite images and 'in situ' air temperature. *Atmos. Res.* 94 (2), 276–284.
- Nichol, J.E., To, P.H., 2012. Temporal characteristics of thermal satellite images for urban heat stress and heat island mapping. *ISPRS J. Photogramm.* 74, 153–162.
- Oke, T.R., 1982. The energetic basis of the urban heat island. *Q. J. Roy. Meteor. Soc.* 1–24. <https://doi.org/10.1002/qj.49710845502>.
- Oke, T.R., 1981. Canyon geometry and the nocturnal urban heat island: comparison of scale model and field observations. *J. Climatol.* 1 (3), 237–254.
- Oke, T.R., Mills, G., Christen, A., Voogt, J., 2017. *Urban climate*. Cambridge University Press.
- Pichierri, M., Bonafoni, S., Biondi, R., 2012. Satellite air temperature estimation for monitoring the canopy layer heat island of Milan. *Remote Sens. Environ.* 127 (4), 130–138. <https://doi.org/10.1016/j.rse.2012.08.025>.
- Qiao, Z., Tian, G., Xiao, L., 2013. Diurnal and seasonal impacts of urbanization on the urban thermal environment: A case study of Beijing using MODIS data. *ISPRS J. Photogramm.* 85, 93–101.
- Quan, J., Chen, Y., Zhan, W., Wang, J., Voogt, J., Wang, M., 2014. Multi-temporal trajectory of the urban heat island centroid in Beijing, China based on a Gaussian volume model. *Remote Sens. Environ.* 149 (7), 33–46. <https://doi.org/10.1016/j.rse.2014.03.037>.
- Quan, L., 2014. Time series analysis and simulation of the surface urban heat island. MSc. Thesis, Cartography and Geographical Information Engineering, University of Electronic Science and Technology of China.

- Quan, J., Zhan, W., Chen, Y., Wang, M., Wang, J., 2016. Time series decomposition of remotely sensed land surface temperature and investigation of trends and seasonal variations in surface urban heat islands. *J. Geophys. Res-Atmos.* 121 (6), 2638–2657.
- Rajasekar, U., Weng, Q.H., 2009. Urban heat island monitoring and analysis using a non-parametric model: A case study of Indianapolis. *ISPRS J. Photogramm.* 64 (1), 86–96.
- Ren, Z., Zhang, Z., Sun, C., Liu, Y., Li, J., Ju, X., Zhao, Y., Li, Z., Zhang, W., Li, H., Zeng, H., Ren, X., Liu, Y., Zeng, X., 2015. Development of three-step quality control system of real time observation data from AWS in China. *Meteorol. Mon.* 41, 1268–1277.
- Runnalls, K.E., Oke, T.R., 2000. Dynamics and controls of the near-surface heat island of Vancouver, British Columbia. *Phys. Geogr.* 21 (4), 283–304.
- Schwarz, N., Lautenbach, S., Seppelt, R., 2011. Exploring indicators for quantifying surface urban heat islands of European cities with MODIS land surface temperatures. *Remote Sens. Environ.* 115 (12), 3175–3186. <https://doi.org/10.1016/j.rse.2011.07.003>.
- Schwarz, N., Manceur, A.M., 2015. Analyzing the influence of urban forms on surface urban heat islands in Europe. *J. Urban Plan. D-ASCE*. 141 (3), A4014003. [https://doi.org/10.1061/\(ASCE\)UP.1943-5444.0000263](https://doi.org/10.1061/(ASCE)UP.1943-5444.0000263).
- Shaposhnikova, M., 2018. The influence of wind speed on night time surface temperatures and the surface urban heat island of Phoenix AZ. MSc. Thesis, Western University, Canada.
- Shen, H., Huang, L., Zhang, L., Wu, P., Zeng, C., 2016. Long-term and fine-scale satellite monitoring of the urban heat island effect by the fusion of multi-temporal and multi-sensor remote sensed data: a 26-year case study of the city of Wuhan in China. *Remote Sens. Environ.* 172, 109–125. <https://doi.org/10.1016/j.rse.2015.11.005>.
- Silva, J.S., da Silva, R.M., Santos, C.A.G., 2018. Spatiotemporal impact of land use/land cover changes on urban heat islands: A case study of Paço de Lumiar, Brazil. *Build. Environ.* 136, 279–292.
- Steenveld, G.J., Koopmans, S., Heusinkveld, B.G., Van Hove, L.W.A., Holtslag, A.A.M., 2011. Quantifying urban heat island effects and human comfort for cities of variable size and urban morphology in the Netherlands. *J. Geophys. Res-Atmos.* 116, D20129. <https://doi.org/10.1029/2011JD015988>.
- Stewart, I.D., Oke, T.R., 2012. Local climate zones for urban temperature studies. *B. Am. Meteorol. Soc.* 93 (12), 1879–1900. <https://doi.org/10.1175/bams-d-11-00019.1>.
- Streutker, D.R., 2002. A remote sensing study of the urban heat island of Houston, Texas. *Int. J. Remote Sens.* 23 (13), 2595–2608.
- Strobl, C., Malley, J., Tutz, G., 2009. An introduction to recursive partitioning: rationale, application, and characteristics of classification and regression trees, bagging, and random forests. *Psychol. Methods* 14 (4), 323. <https://doi.org/10.1037/a0016973>.
- Theeuwes, N.E., Steenveld, G.J., Ronda, R.J., Holtslag, A.A., 2017. A diagnostic equation for the daily maximum urban heat island effect for cities in northwestern Europe. *Int. J. Climatol.* 37 (1), 443–454.
- Tran, H., Uchihama, D., Ochi, S., Yasuoka, Y., 2006. Assessment with satellite data of the urban heat island effects in Asian mega cities. *Int. J. Appl. Earth Obs.* 8 (1), 34–48. <https://doi.org/10.1016/j.jag.2005.05.003>.
- Tran, D.X., Pla, F., Latorre-Carmona, P., Myint, S.W., Caetano, M., Kieu, H.V., 2017. Characterizing the relationship between land use land cover change and land surface temperature. *ISPRS J. Photogramm.* 124, 119–132.
- Voogt, J.A., 2008. Assessment of an urban sensor view model for thermal anisotropy. *Remote Sens. Environ.* 112 (2), 482–495. <https://doi.org/10.1016/j.rse.2007.05.013>.
- Voogt, J.A., Oke, T.R., 2003. Thermal remote sensing of urban climates. *Remote Sens. Environ.* 86 (3), 370–384. [https://doi.org/10.1016/s0034-4257\(03\)00079-8](https://doi.org/10.1016/s0034-4257(03)00079-8).
- Vapnik, V., 1995. *The nature of statistical learning theory*. Springer, New York.
- Wan, Z., 2008. New refinements and validation of the MODIS land-surface temperature/emissivity products. *Remote Sens. Environ.* 112 (1), 59–74. <https://doi.org/10.1016/j.rse.2006.06.026>.
- Wang, J., Huang, B., Fu, D., Atkinson, P., 2015. Spatiotemporal variation in surface urban heat island intensity and associated determinants across major Chinese cities. *Remote Sens.* 7 (4), 3670–3689.
- Wang, K., Jiang, S., Wang, J., Zhou, C., Wang, X., Lee, X., 2017. Comparing the diurnal and seasonal variabilities of atmospheric and surface urban heat islands based on the Beijing urban meteorological network. *J. Geophys. Res-Atmos.* 122 (4), 2131–2154. <https://doi.org/10.1002/2016JD025304>.
- Ward, K., Lauf, S., Kleinschmit, B., Endlicher, W., 2016. Heat waves and urban heat islands in Europe: A review of relevant drivers. *Sci. Total Environ.* 569–570, 527–539. <https://doi.org/10.1016/j.scitotenv.2016.06.119>.
- Weng, Q., Lu, D., Schubring, J., 2004. Estimation of land surface temperature–vegetation abundance relationship for urban heat island studies. *Remote Sens. Environ.* 89 (4), 467–483.
- Weng, Q.H., 2009. Thermal infrared remote sensing for urban climate and environmental studies: Methods, applications, and trends. *ISPRS J. Photogramm.* 64 (4), 335–344. [https://doi.org/10.1016/S0924-2716\(03\)00016-9](https://doi.org/10.1016/S0924-2716(03)00016-9).
- Weng, Q., Fu, P., 2014. Modeling diurnal land temperature cycles over Los Angeles using downscaled GOES imagery. *ISPRS J. Photogramm.* 97, 78–88.
- Xu, H., Shi, T., Wang, M., Fang, C., Lin, Z., 2018. Predicting effect of forthcoming population growth-induced impervious surface increase on regional thermal environment: Xiong'an New Area, North China. *Build. Environ.* 136, 98–106.
- Yang, J., Wong, M.S., Menenti, M., Nichol, J., 2015. Study of the geometry effect on land surface temperature retrieval in urban environment. *ISPRS J. Photogramm.* 109, 77–87.
- Yang, Q., Huang, X., Li, J., 2017. Assessing the relationship between surface urban heat islands and landscape patterns across climatic zones in China. *Sci. Rep.* 7 (1), 9337. <https://doi.org/10.1038/s41598-017-09628-w>.
- Yang, Q., Huang, X., Tang, Q., 2019. The footprint of urban heat island effect in 302 Chinese cities: Temporal trends and associated factors. *Sci. Total Environ.* 655, 652–662.
- Yao, R., Wang, L., Gui, X., Zheng, Y., Zhang, H., Huang, X., 2017. Urbanization effects on vegetation and surface urban heat islands in China's Yangtze River Basin. *Remote Sens.* 9 (6), 540. <https://doi.org/10.3390/rs9060540>.
- Zhang, X., Steenveld, G.J., Zhou, D., Duan, C., Holtslag, A.A., 2019. A diagnostic equation for the maximum urban heat island effect of a typical Chinese city: A case study for Xi'an. *Build. Environ.* 158, 39–50.
- Zhao, L., Lee, X., Smith, R.B., Oleson, K., 2014. Strong contributions of local background climate to urban heat islands. *Nature* 511 (7508), 216–219.
- Zhao, L., Oppenheimer, M., Zhu, Q., Baldwin, J.W., Ebi, K.L., Bou-Zeid, E., Guan, K., Liu, X., 2018. Interactions between urban heat islands and heat waves. *Environ. Res. Lett.* 13 (3), 034003.
- Zheng, J., Yin, Y., Li, B., 2010. A new scheme for climate regionalization in China. *Acta Geograph. Sin.* 65 (1), 3–13.
- Zhou, B., Rybski, D., Kropp, J.P., 2013. On the statistics of urban heat island intensity. *Geophys. Res. Lett.* 40 (20), 5486–5491. <https://doi.org/10.1002/2013GL057320>.
- Zhou, B., Rybski, D., Kropp, J.P., 2017. The role of city size and urban form in the surface urban heat island. *Sci. Rep.* 7 (1), 4791. <https://doi.org/10.1038/s41598-017-04242-2>.
- Zhou, D., Zhao, S., Liu, S., Zhang, L., Zhu, C., 2014a. Surface urban heat island in China's 32 major cities: Spatial patterns and drivers. *Remote Sens. Environ.* 152, 51–61. <https://doi.org/10.1016/j.rse.2014.05.017>.
- Zhou, D., Zhang, L., Li, D., Huang, D., Zhu, C., 2016. Climate-vegetation control on the diurnal and seasonal variations of surface urban heat islands in China. *Environm. Res. Lett.* 11 (7), 074009.
- Zhou, D., Xiao, J., Bonafoni, S., Berger, C., Deilami, K., Zhou, Y., Frolking, S., Yao, R., Qiao, Z., Sobrino, J., 2019. Satellite remote sensing of surface urban heat islands: Progress, challenges, and perspectives. *Remote Sens.* 11 (1), 48. <https://doi.org/10.3390/rs11010048>.
- Zhou, J., Chen, Y.H., Wang, J.F., Zhan, W.F., 2011. Maximum nighttime urban heat island (UHI) intensity simulation by integrating remotely sensed data and meteorological observations. *IEEE J-STARS.* 4 (1), 138–146.
- Zhou, W., Qian, Y., Li, X., Li, W., Han, L., 2014b. Relationships between land cover and the surface urban heat island: seasonal variability and effects of spatial and thematic resolution of land cover data on predicting land surface temperatures. *Landscape Ecol.* 29 (1), 153–167.